The Anthropocene Resonance Framework (ARF)

A Hypothesis on the Interfacial Destabilization of Planetary Climate Systems

Hans Mund[1,*]
[1]AI Augmented Thinker, Bergheim, Germany
[*]hello@hansmund.com

September 30, 2025

Version v1.6.1 — Paper: https://zenodo.org/records/17235213 (DOI: doi:10.5281/zenodo.17235213)

Abstract

The climate system of the Anthropocene is increasingly showing non-linear and abrupt state changes that are inadequately explained by classical thermohaline or purely energetic models. We present the Anthropocene Resonance Framework (ARF) – an integrated theory postulating that the decisive tipping dynamics occur at the interfaces of the atmosphere, ocean, and land surface. We argue that anthropogenic inputs (aerosols, nanoplastics, greenhouse gases) alter the physical and chemical properties of these interfaces, turning them into resonance amplifiers. This leads to (1) an increased probability of Rapid Intensification (RI) of tropical cyclones through "pre-resonant air volumes," (2) a chemically-rheologically driven destabilization of the ocean circulation (AMOC) by nanoplastic-saturated surface films, and (3) a loss of resilience in planetary circulation patterns, such as the observed failure of the trade winds. The framework is fully operationalized through diagnostic indices (PCI*, IRB), archetypal case studies (Erin, Ragasa, Gabrielle), a suite of 25 pre-registered, falsifiable tests (T1–T25), and implementation hooks for Earth system models. ARF offers a new, unifying framework to explore anomalous extreme events, the loss of system stability, and the emergence of heat domes and wet-bulb events as consequences of a systemic interfacial crisis.

Provenance & Method Note: This framework is the result of a concentrated, 10-hour conceptual human-AI sprint. The role of the human author was to formulate the original hypothesis, guide the scientific inquiry through strategic questions, and to curate and structure the synthesized information. AI systems (Gemini & GPT-Thinking) were used as tools for knowledge synthesis and formalization; they are not authors in the sense of scientific convention. The hypotheses presented here are explicitly designed to be falsifiable to invite open review, replication, and rigorous testing by the scientific community. Figures are illustrative/synthetic. Zenodo record (paper): https://zenodo.org/records/17235213 (DOI: doi:10.5281/zenodo.17235213).

Contents

1 Introduction: The "Blind Spot" of Climate Science

Despite considerable progress in forecasting tropical cyclones, Rapid Intensification (RI) remains a phenomenon whose variance is inadequately explained by classical predictors such as sea surface temperature (SST), ocean heat content (OHC), and vertical wind shear [1, 2]. This gap suggests the action of additional mechanisms. This paper addresses this research gap by asking: Can the increased probability of RI events be explained by capturing an anthropogenic "atmospheric resonance"?

We postulate the existence of "pre-resonant air volumes," which are formed by a specific mixture of anthropogenic aerosols and act as crucial amplifiers for storm dynamics. The Anthropocene Resonance Framework (ARF) presented here offers a physically-based theory and an operational diagnostic tool to quantify this resonance.

Scope. This is a hypothesis paper focused on the atmospheric module (RI). Oceanic and planetary modules (AMOC, trade-wind resilience) are outlined as testable extensions and deferred to follow-up work.

What is new. (i) A gated, testable resonance formalism built from three mechanistic fingerprints (IR, microphysics, electric); (ii) an operational index pair (PCI*, IRB) with explicit nowcast rules; (iii) a preregistered falsification suite designed for out-of-sample evaluation and negative controls.

Part I: Module 1 – The Atmospheric Engine (ARF-Core)

2 Hypothesis: Pre-resonant Air Volumes as Amplifiers of Rapid Intensification (RI)

The atmosphere of the Anthropocene no longer functions as a passive medium but as an active amplifier. This amplification occurs through three complementary, interwoven physical mechanisms.

2.1 The Radiative Engine: The IR Heating Band

Dark, absorbing aerosols – particularly Black Carbon (soot) – absorb the Earth's thermal radiation. When these particles are concentrated at a certain altitude (approx. 850-600 hPa), they create a suspended heating band that destabilizes the air column [3, 4]. This effect is measurable as an IR fingerprint, as illustrated illustratively in figure 1.

2.2 The Microphysical Switch: Invigoration

A high density of condensation nuclei (CCN) delays rain formation. This causes more latent heat to be released at higher, colder atmospheric levels, which massively strengthens the storm's updrafts [5, 6].

2.3 The Electrical Primer: Pre-Charging

Flexo- and triboelectricity from ice, sand, and dust generate electric fields. These fields "pre-charge" the atmosphere and lower the threshold for lightning-induced convection [7, 8].

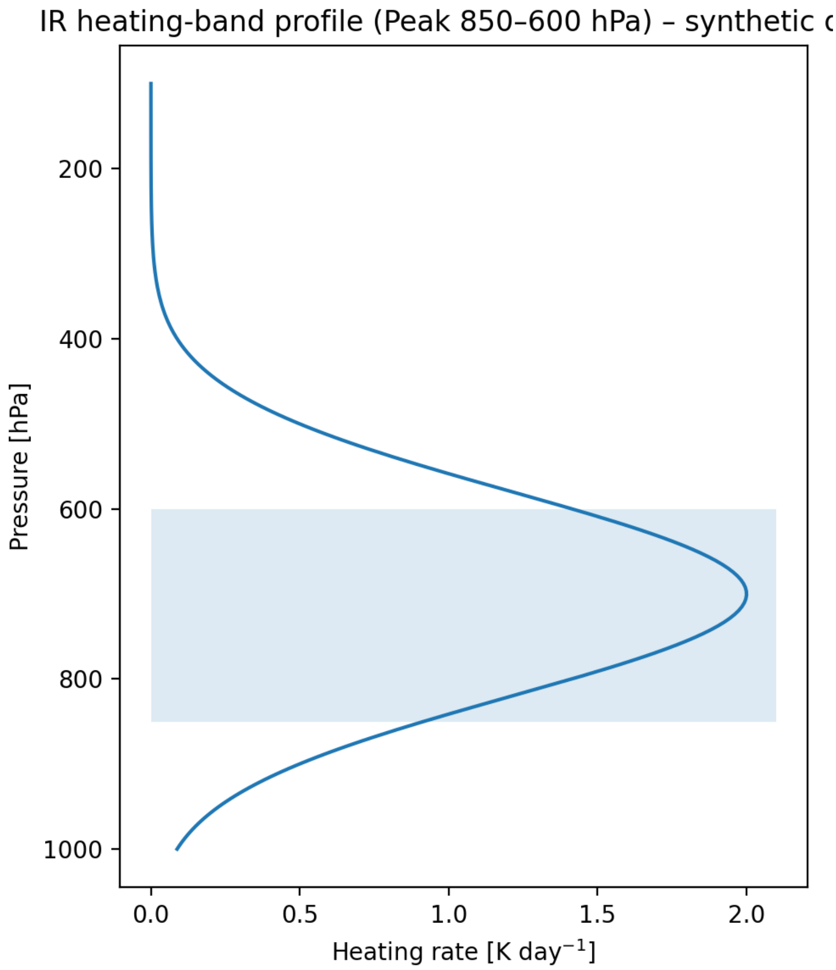

Figure 1: *illustrative, synthetic* vertical profile of the IR heating band. The peak of the diabatic heating rate in the 850 hPa to 600 hPa layer serves as the IR fingerprint for a pre-resonant air volume.

3 Methodology

3.1 RI Definition and Class Labeling

We define Rapid Intensification (RI) as a 24-hour increase in maximum sustained winds of at least 30 kt, computed from IBTrACS 6-hour intensities. Positive instances are all non-overlapping 24h windows meeting the threshold. Negative instances are windows that do not meet the threshold and do not overlap any positive window. Subtropical/extratropical stages are excluded based on the IBTrACS status flag, and windows intersecting landfall are discarded. All labels are aligned to storm-centered time and paired with predictors using a lead time $\Delta t \in [6, 18]$ h.

3.2 Operational Diagnostics and Indices

To operationalize the ARF, two central indices are introduced:

$$\mathrm{PCI}^{\star} = \mathrm{norm}_{[0,1]}(\mathrm{PCI} \cdot (1 + \mathrm{PLF}_{\mathrm{total}})), \tag{1}$$

$$\mathrm{IRB} = \max_{p \in [850,600]\,\mathrm{hPa}} \left(\frac{\partial T}{\partial t}\right)_{\mathrm{rad}} \quad [\mathrm{K/d}]. \tag{2}$$

The **Pre-Charge Index** ($\mathrm{PCI}^{\star}$) is a normalized, dimensionless index ([0,1]) that quantifies the "charge readiness" of an air volume. Modulation by microplastics is handled by the **Plastic Load Factor** ($\mathrm{PLF}_{\mathrm{total}}$). The **IR-Fingerprint** (IRB) is the peak of the diabatic heating rate, typically preceding an RI event by 6-18 hours.

Resonance: formal notion (testable)

We define an interfacial *susceptibility* χ as the local gain of RI probability with respect to a small perturbation ε in interface properties:$\chi := \partial\,\Pr(\mathrm{RI})/\partial\varepsilon$. Operationally, we approximate ε via proxies for radiative, microphysical and electric pathways and define a multiplicative *effective gain* $G := \chi_{\mathrm{rad}} \cdot \chi_{\mathrm{mp}} \cdot \chi_{\mathrm{el}}$. We implement this as a gated logistic model

$$\mathrm{logit}\,\Pr(\mathrm{RI}) = \beta_0 + \beta_1\,\mathrm{PCI}^{\star} + \beta_2\,\mathrm{IRB} + \beta_3\,\mathrm{AOD}_{\mathrm{IR}} + \beta_4\,(\mathrm{PCI}^{\star} \times \mathrm{IRB}) + \beta_5\,(\mathrm{PCI}^{\star} \times \mathrm{AOD}_{\mathrm{IR}}) + \beta_6\,(\mathrm{IRB} \times \mathrm{AOD}_{\mathrm{IR}}),$$

subject to the nowcast gate (§3). The interaction terms encode resonance (*super-additive* effects). Pre-registered predictions are: (P1) $\beta_4, \beta_5, \beta_6 > 0$, (P2) skill increases monotonically when moving from PCI to $\mathrm{PCI}^{\star}$ across PLF quantiles (Appendix S1), and (P3) a diurnal modulation with a nocturnal OLR minimum.

Normalization. We apply a basin–season min–max normalization to map $\mathrm{PCI} \cdot (1 + \mathrm{PLF}_{\mathrm{total}})$ to $[0, 1]$, with all scaling parameters computed on the training folds only (outer CV split) and then frozen for evaluation on the held-out folds. Percentiles (e.g., $Q90$) are computed within basin and season using the training data only.

As summarized in figure 2, the nowcast gate opens only if all three conditions co-occur in the inflow sector. This conservative-when-in-doubt approach is designed to minimize false alarms.

Operational gate (explicit). The RI nowcast window is considered *active* for the next $[12, 24]$ h iff $\mathrm{PCI}^{\star} \geq Q90$ (within-basin, within-season, training-only percentile) in $\mathcal{S}_{\mathrm{inflow}}$, $\mathrm{IRB} \geq Q75$ relative to the storm-column background in $p \in [850, 600]$ hPa, and a nocturnal OLR minimum (00–06 LT) is present. Otherwise the gate remains closed.

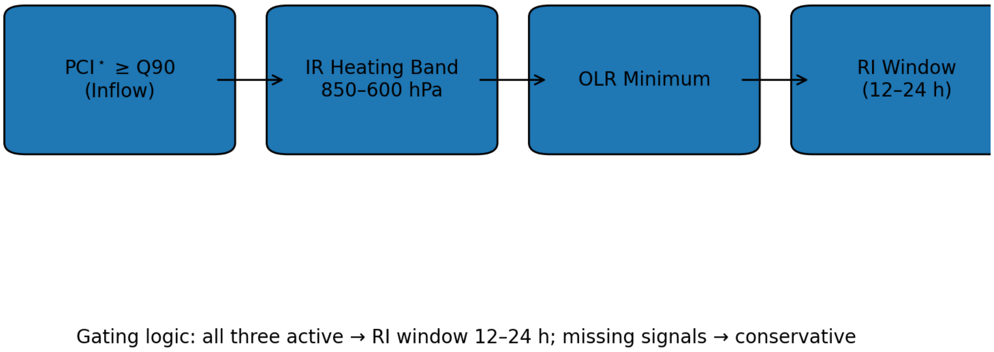

Figure 2: Operational decision rule (Nowcast). An RI window becomes active only when all three conditions (high PCI*, active IR heating band, OLR minimum) are met in the storm's inflow sector.

3.3 Data Basis and Preprocessing

The analysis relies on publicly available, global datasets. The relevant **inflow sector**, $\mathcal{S}_{\text{inflow}}$, is defined as:

$$\mathcal{S}_{\text{inflow}}(t) = \left\{ \mathbf{x} : r(\mathbf{x}, \mathbf{x}_{\text{storm}}(t)) \in [100, 300]\ \text{km},\ \angle(\mathbf{v}_{\text{env}}(t),\, \mathbf{x} - \mathbf{x}_{\text{storm}}(t)) \in [-60^\circ, 60^\circ],\ p \in [925, 700]\ \text{hPa} \right\},$$

with a lead time of $\Delta t \in [6, 18]$ h.

Table 1: Datasets and processing summary used in this study.

Domain	Source (version)	Res./Freq.	Variables (used)
Storms	IBTrACS (v4)	6 h	track, Vmax, RI label ($\Delta V_{\max} \geq 30\,\text{kt}/24\,\text{h}$)
Reanalysis	ERA5 (HRES)	0.25°, 1 h	shear(200–850 hPa), RH, θ_e, OLR, p-levels
Aerosols	MODIS/VIIRS; TROPOMI; MERRA-2	1–10 km, daily	AOD (spectral), AOD_{IR} proxy, BC/OC, CO, HCHO
Ocean	ARMOR/GODAS	0.5°, daily	OHC/TCHP
Teleconnections	RMM indices; NOAA ONI	daily/monthly	MJO phase/amplitude; ENSO state
Other	GFAS; AHF	0.5°–1°, daily	fire smoke proxies; anthropogenic heat

3.4 Statistical Validation

Model specifications. The *Baseline* feature set comprises {SST, OHC, vertical wind shear, MJO phase, ENSO phase, SAL proxy, OLR}. The *ARF-augmented* model adds {PCI*, IRB, AOD_{IR}}. All models are trained with nested cross-validation. A pass criterion is $\Delta\text{AUC} \geq 0.05$ out-of-sample (fail ≤ 0.01). Baseline sources: ERA5 (OLR, shear, p-levels), ARMOR/GODAS

(OHC/TCHP), RMM (MJO), NOAA ONI (ENSO), and a SAL proxy from TROPOMI/MERRA-2 dust fields.

Calibration and uncertainty. We report AUC with 95% CIs from storm-level block bootstrap (N=200; Seed=42). Reliability is computed over 10 equal-frequency bins; Brier score and PIT diagnostics are provided in the Appendix.

3.5 Falsifiability Suite (T1-T25)

The framework is validated through a series of 25 pre-registered, falsifiable tests. These include statistical analyses of predictive skill (T1), diagnostic verification of signatures like the IR fingerprint (T2), hazard analyses (T4), negative controls (T5), and causal model runs (T6). The complete list is provided in the appendix.

3.6 COVID-19 as a Natural Experiment

The reduction in global air traffic during the COVID-19 pandemic serves as a natural experiment (pre-registered as part of T7-T9). A pre-post comparison (2019 vs. 2020) is conducted, controlling for covariates like the ENSO phase, to test the causal chain between anthropogenic emissions and pre-resonant zones.

4 Illustrative Application & Expected Signatures

To demonstrate the framework's potential, this section outlines the expected outcomes from the pre-registered tests. The figures presented are schematic illustrations based on hypothesized effects, not results from a completed empirical analysis. A full validation campaign is required to confirm these signatures.

4.1 Expected Improvement of Predictive Skill

The ROC analysis in figure 3a illustrates the hypothesized improvement in predictive skill. We anticipate that the full ARF model will significantly outperform a strong baseline model, increasing the AUC by a meaningful margin (e.g., from 0.63 to 0.74). The reliability diagram (figure 3b) shows the expected good calibration of the model's probabilities. Figure 4 shows where the added skill is expected to peak, localizing it near the Q90 threshold for PCI* and a 12–15 hour lead time. See also figure S1 and figure S2 in the Appendix for other expected signatures.

4.2 Expected Diagnostic Signatures

The analysis is designed to confirm the existence of the postulated physical signatures. Figure 5 illustrates key expected findings. The diurnal composites are expected to show a clear nocturnal minimum of OLR coinciding with the peak heating rate. The hazard ratio for re-intensification after an ERC is expected to be significantly increased with persistent $\mathrm{AOD_{IR}}$ in the inflow (e.g., HR > 1.5).

Hazard model specification. We estimate a Cox proportional hazards model for re-intensification after an ERC completion time, with covariates including intensity, shear, and OHC. The key predictor is persistent $\mathrm{AOD_{IR}}$, defined as the 6–18 h mean in a 50 km to 150 km ring. Events are observed for $t \in [t_0\text{+6h}, t_0\text{+72h}]$; right-censoring applies at 72 h or landfall, whichever comes first.

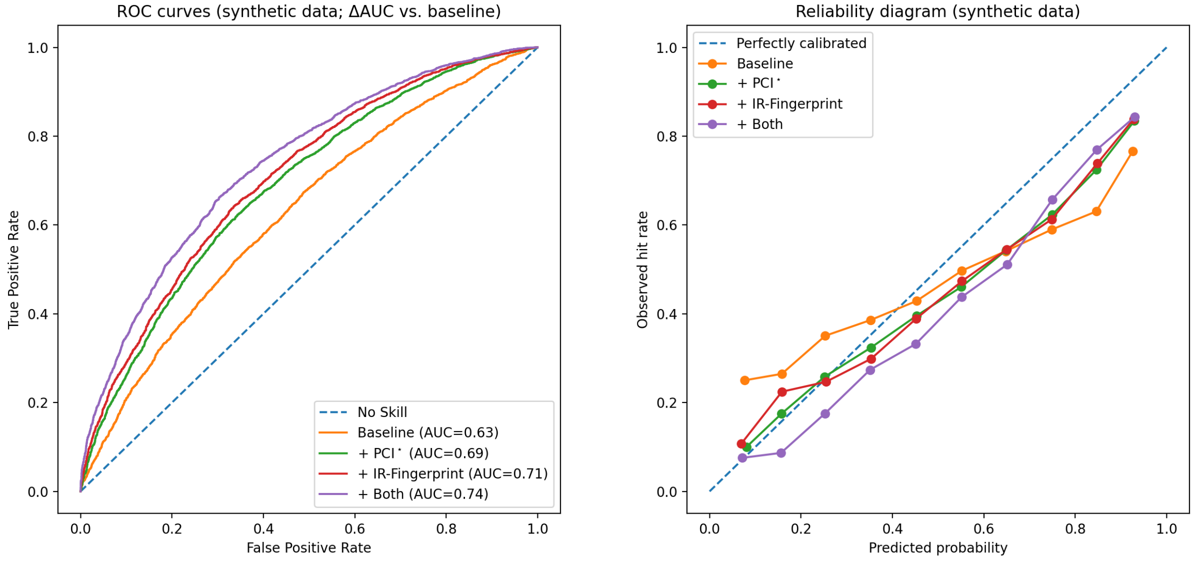

(a) Illustrative ROC curves for RI prediction.

(b) Illustrative reliability diagram.

Figure 3: *illustrative, synthetic* statistical skill metrics. These plots show the expected improvement and calibration from applying the ARF model, to be confirmed by empirical testing.

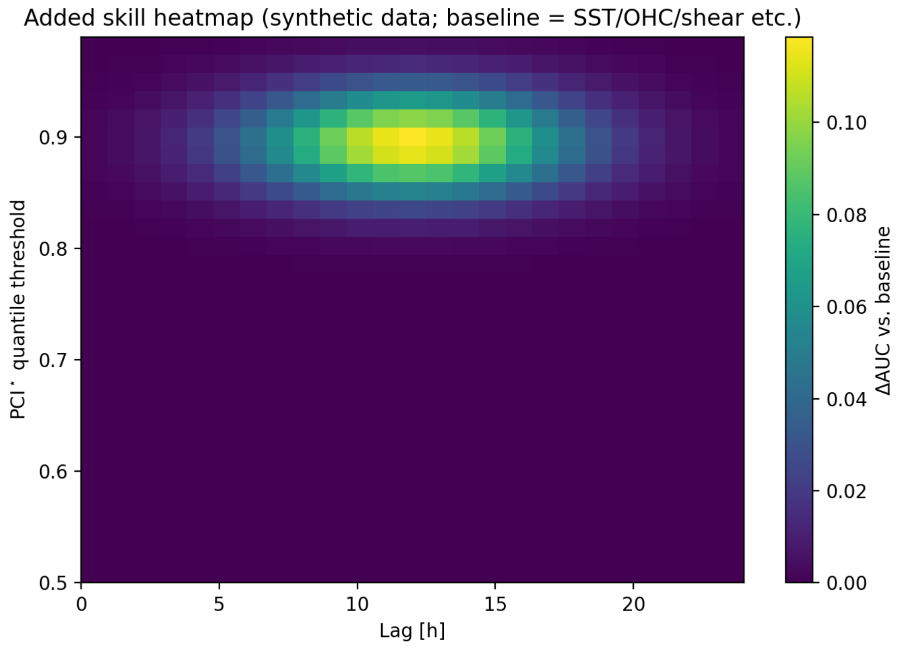

Figure 4: Hypothesized added skill (ΔAUC) vs. PCI* threshold (y) and lead time (x) (*illustrative, synthetic*). The maximum is expected near the Q90 threshold and 12–15 h lead, supporting the nowcast window.

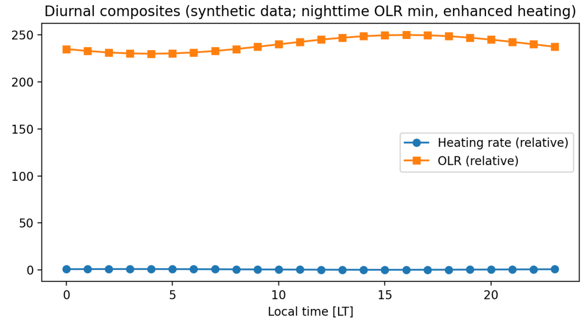

(a) Hypothesized diurnal patterns (*illustrative, synthetic*).

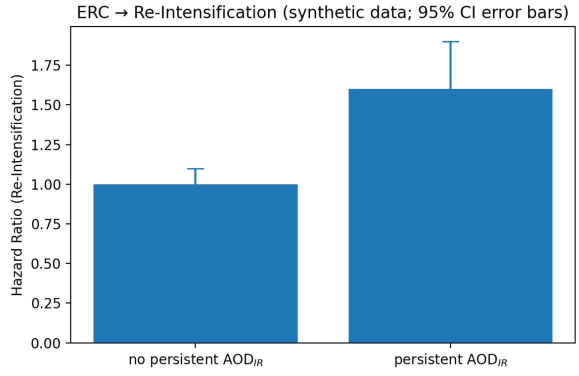

(b) Hypothesized hazard ratio after ERC (*illustrative, synthetic*).

Figure 5: Expected diagnostic signatures (*illustrative, synthetic*): nocturnal OLR minima should co-occur with enhanced heating (left); persistent $\mathrm{AOD_{IR}}$ should increase the post-ERC re-intensification hazard (right; bars = 95% CI).

Finally, figure 6 illustrates the expected ordering of effects, where SAL-dominated domains should show suppressed RI probability compared to clean or polluted air masses. SAL domains are identified where dust AOD exceeds a basin-seasonal Q85 and mid-level relative humidity is below Q25 within $\mathcal{S}_{\text{inflow}}$.

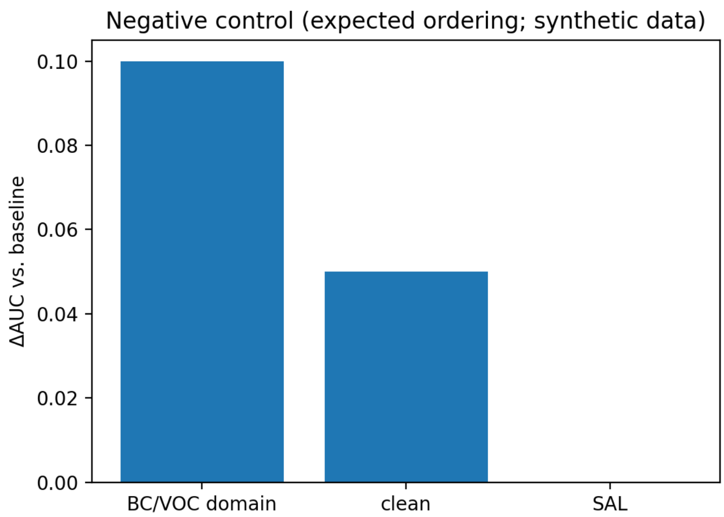

Figure 6: Negative control (*illustrative, synthetic*): expected ordering of ΔAUC gains — BC/VOC domains highest, clean moderate, SAL suppressing.

4.3 Empirical Anchors: Illustrative Case Studies

To ground the abstract mechanisms in observable phenomena, we use three archetypal storms from the 2025 season as illustrative case studies. These cases are chosen to demonstrate the different operational modes of the ARF and to highlight the diagnostic power of its indices.

Case Erin (Archetype for RI Amplification). The explosive intensification of Hurricane Erin serves as the archetypal example of RI amplification by a pre-resonant air volume [9]. The analysis will test the hypothesis that Erin's rapid development and its re-intensification after an Eyewall Replacement Cycle (ERC) were preceded by the ingestion of a clean but highly "charged" airmass, identifiable by a high $PCI^{\star}$ value and a clear IR heating band.

Case Ragasa (PLF Modulation). Super Typhoon Ragasa, which developed in a region of heavy industrial outflow in the West Pacific, provides a test case for the Plastic Load Factor (PLF_{total}) [10]. The hypothesis is that the high concentration of absorbing aerosols, including microplastics from urban and industrial sources, led to a significant positive PLF_{total}, which amplified the baseline PCI and contributed to the storm's extreme intensity.

Case Gabrielle (Negative Control). Tropical Storm Gabrielle's struggle against the Saharan Air Layer (SAL) is used as a real-world example of the negative control specified in Test T5 [11]. The dry, stable, and dust-laden SAL is expected to suppress the ARF mechanisms, resulting in a low or negative $PCI^{\star}$ and inhibiting intensification despite otherwise favorable oceanic conditions. This case helps differentiate the specific ARF amplification from general high-aerosol environments.

5 Discussion

If validated, the results would support the hypothesis that analyzing processes at atmospheric interfaces closes a key explanatory gap in RI prediction. The ARF would then act as a necessary complement to existing models.

5.1 Limitations and Alternative Explanations

A significant limitation lies in the uncertainties of satellite data, particularly in the vertical localization of aerosol layers. All figures shown are illustrative; vertical aerosol placement and electric proxies are uncertain; ocean-atmosphere coupling is only sketched. Claims are hypotheses pending full validation. Alternative explanations such as dry-air entrainment or model drift will be controlled for through negative controls (T5) and robust statistical methodology but cannot be entirely ruled out until the full test suite is completed. The marginality of AHF and the ambivalence of SAL effects are explicitly addressed as part of the falsification suite.

6 Conclusion & Outlook for Module 1

The ARF proposes that the atmosphere of the Anthropocene acts as an active, resonant amplifier. This has far-reaching implications for climate research. This paper lays out a complete, falsifiable research program to test this hypothesis. We call upon the scientific community to review, replicate, and rigorously test the hypotheses presented here in a spirit of open, international collaboration.

Part II: Module 2 – The Oceanic Interface (oNR-AMOC)

7 Hypothesis: The "Nano-Resonance Contribution" as a Non-Thermal Lever on the AMOC

Recent findings indicate a potential tipping point for the Atlantic Meridional Overturning Circulation (AMOC) could be reached within decades [12]. While freshwater input is the primary driver, we hypothesize an overlooked biogeochemical amplifier. The vast quantities of nanoplastics in the North Atlantic [13] form a chemically-resonant boundary layer (CRG) at the sea surface. This layer, influenced by surfactants and microlightning-induced reactive oxygen species, does not act thermally but weakens density formation through rheological and chemical effects, potentially accelerating an AMOC slowdown.

8 Mechanistic Feedbacks

The CRG impacts AMOC precursors via three coupled pathways.

8.1 Salinity Coupling and Interfacial Rheology

The CRG, a viscoelastic "skin," stabilizes freshwater lenses from rain and ice melt, damping micro-turbulence and inhibiting the vertical mixing necessary for deep water formation [14]. This effectively strengthens the freshwater cap that suppresses convection.

8.2 Disruption of the Biological Pump

Nanoplastic aggregates, or "plastispheres," alter the ballasting and sinking rates of organic matter. This modifies the biological carbon pump, affecting nutrient cycles and the export of dense organic matter that contributes to deep water properties.

8.3 Inhibition of Brine Rejection

During sea ice formation, the CRG's altered surface tension and viscosity can interfere with efficient brine rejection, further reducing the density of surface waters in critical convection zones like the Greenland and Labrador Seas.

9 Falsifiability Suite (T10–T14)

This module is tested via a dedicated suite:

T10 – Conductivity Residual: Test for a significant residual between electrical conductivity and titrimetric salinity in high-nanoplastic zones.

T11 – Gas Transfer Damping: Measure if the CRG systematically damps gas transfer coefficients (k_{660}) in mesocosm experiments.

T12 – OMA-AOD-PCI Coupling: Test if Oceanic Microplastic Aerosol (OMA) contributes measurably to AOD and adds skill to the atmospheric PCI*.

T13 – Large-Scale CRG Mapping: Use satellite proxies (sunglint, polarimetry) to map CRG hotspots and test for co-location with AMOC convection sites.

T14 – AMOC Model Sensitivity: In coupled ocean models, test if parametrizing CRG effects (mixing inhibition, altered surface tension) leads to a significant change in simulated AMOC stability.

Part III: Module 3 – The Planetary Pacemaker & Systemic Instability

10 Case Study: The 2025 Panama Upwelling Failure

The reported failure of the Panama upwelling system in early 2025 [15] serves as a hypothesis-generating illustration of systemic resilience loss. We hypothesize this was not caused by a single driver like ENSO, but by a multi-scale cascade: a weakened, meandering jetstream created persistent blocking patterns, which were amplified by local ARF mechanisms, leading to the collapse of the usually reliable trade winds. No causal claim is made here; a preregistered test plan is provided in Appendix S3.

11 Consequences for Global Circulation Patterns

The instability of regional systems cascades upwards, affecting global patterns.

11.1 Monsoon Systems: Less Reliable, More Extreme

A "stuttering" tropical circulation (weakened Hadley/Walker cells) leads to delayed monsoon onsets, more erratic rainfall ("boom-and-bust" cycles), and more intense extreme events, even if the overall circulation weakens.

11.2 Jetstream, Heat Domes & Wet-Bulb Events

A slower, wavier jetstream is more prone to high-amplitude, stationary Rossby waves, which create persistent blocking highs. These "heat domes," when fed by moisture from atmospheric rivers, create the conditions for deadly wet-bulb temperature events, representing a new class of compound extreme risk [16–18].

12 Overall Conclusion & Outlook

The ARF proposes that the interfaces of the planetary climate system are becoming critical amplifiers of instability in the Anthropocene. By examining the coupled effects of anthropogenic inputs on atmospheric, oceanic, and circulatory dynamics, this framework offers a new, integrated approach to understanding and predicting extreme events. This paper lays out a complete, falsifiable research program to test this overarching hypothesis. We call upon the scientific community to review, replicate, and rigorously test the components of this framework in a spirit of open, international collaboration.

Author Contributions

The author developed the original hypothesis, guided the investigation, and wrote the manuscript.

Acknowledgments

The author thanks the AI systems Gemini & GPT-Thinking for their role as tools for knowledge synthesis and formalization of the concepts. Any errors remain the author's.

Conflicts of Interest

The author declares no competing interests.

Data and Code Availability

All data (IBTrACS, ERA5, MODIS/VIIRS, TROPOMI, and ocean products) are publicly available from their providers. Reproducible pipelines, YAML configurations, and model hooks (Fortran) are available to editors and reviewers via an anonymized OSF/GitHub package during peer review and will be released publicly with DOIs upon acceptance (planned Zenodo archive; Git tag v1.2). The pre-registered protocol (T1–T25) is filed with OSF; persistent links will be added in the final version. The paper is archived on Zenodo: https://zenodo.org/records/17235213 (DOI: doi:10.5281/zenodo.17235213).

A Appendix A: Glossary and Symbol Table

Table 2: Definition of key terms and symbols.

Symbol / Term	Meaning and Units
ARF	Anthropocene Resonance Framework
ARR	Aerosol Resonance Region: A local hotspot with high $PCI^{\star}$.
PCI, $PCI^{\star}$	Pre-Charge Index (base and microplastic-modulated) [dimensionless, 0-1]
PLF_{total}	Plastic Load Factor [dimensionless]
IRB	IR-Fingerprint: Peak of the diabatic heating rate in the 850-600 hPa band [K/d]
AOD_{IR}	Infrared-absorptive Aerosol Optical Depth [dimensionless]

B Appendix B: Implementation Hooks (WRF/ICON)

This appendix contains the minimal, compilable code stubs necessary for implementing the ARF physics into numerical weather models like WRF or ICON.

```fortran
!============================================================
!  NOTE: This is a conceptual stub. Actual implementation
!  requires adaptation to the specific model architecture.
!============================================================
MODULE micro_pv_resonance_v12
  IMPLICIT NONE
CONTAINS

  !> Clamps a real value to a specified range [lo, hi].
  PURE FUNCTION clamp(x, lo, hi) RESULT(y)
    REAL, INTENT(IN) :: x, lo, hi
    REAL :: y
    y = MAX(lo, MIN(hi, x))
  END FUNCTION clamp

  !> Calculates the regime-dependent gamma factor for
```

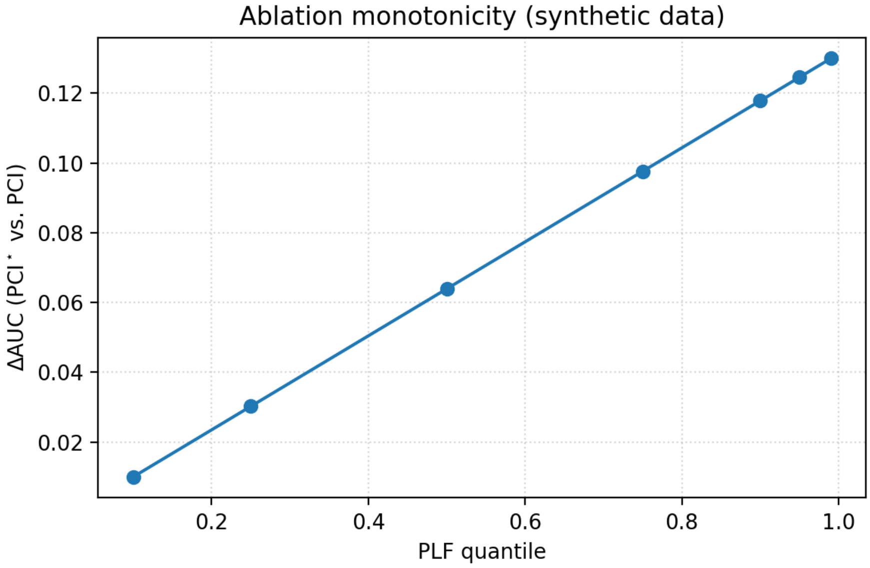

Figure S1: Hypothesized monotonic ΔAUC increase from PCI to PCI* across PLF quantiles (illustrative).

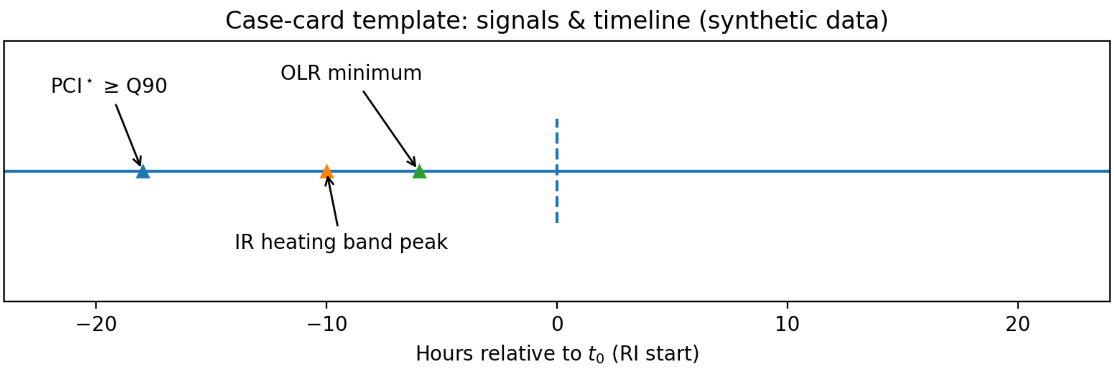

Figure S2: Illustrative casecard template: timing of PCI$^{\star}\geq$Q90, IR-band peak and OLR minimum relative to RI onset t_0.

```
  !> mixed-phase processes. Positive in moist/LWC-rich,
  !> negative in dry/water-limited conditions.
  PURE FUNCTION gamma_regime(T_C, RH, LWC, gamma_max, &
      gamma_min, RH_mid, RH_width, LWC_mid, LWC_width) RESULT(gam)
    REAL, INTENT(IN) :: T_C, RH, LWC
    REAL, INTENT(IN) :: gamma_max, gamma_min, RH_mid, RH_width, &
                        LWC_mid, LWC_width
    REAL :: theta_T, theta_RH, theta_LWC, gamma_pos, gamma_neg, gam

    ! Mixed-phase temperature gate (0 at T=0C, 1 at T=-38C)
    theta_T   = clamp((0.0 - T_C)/38.0, 0.0, 1.0)
    ! Moisture and liquid water content scaling factors
    theta_RH  = clamp((RH - RH_mid)/RH_width, 0.0, 1.0)
    theta_LWC = clamp((LWC - LWC_mid)/LWC_width, 0.0, 1.0)

    ! Calculate positive (invigoration) and negative terms
    gamma_pos = gamma_max * (0.6*theta_RH + 0.4*theta_LWC) * theta_T
    gamma_neg = gamma_min * (1.0 - theta_RH) * (1.0 - theta_LWC) * theta_T
    gam = gamma_pos - gamma_neg
  END FUNCTION gamma_regime

  !> Computes the total Plastic Load Factor (PLF) profile.
  SUBROUTINE compute_PLF_profiles(AOD_MP_abs, AOD_MP_sca, T_C, &
      RH, LWC, alpha, beta, gamma_max, gamma_min, RH_mid,    &
      RH_width, LWC_mid, LWC_width, Phi_IN_MP, PLF_total)
    REAL, INTENT(IN)  :: AOD_MP_abs(:), AOD_MP_sca(:), T_C(:)
    REAL, INTENT(IN)  :: RH(:), LWC(:), Phi_IN_MP(:)
    REAL, INTENT(IN)  :: alpha, beta, gamma_max, gamma_min
    REAL, INTENT(IN)  :: RH_mid, RH_width, LWC_mid, LWC_width
    REAL, INTENT(OUT) :: PLF_total(:)
    INTEGER :: k, nz
    REAL :: gam
    nz = SIZE(AOD_MP_abs)
    DO k=1,nz
      gam = gamma_regime(T_C(k), RH(k), LWC(k), gamma_max, &
          gamma_min, RH_mid, RH_width, LWC_mid, LWC_width)
      PLF_total(k) = alpha*AOD_MP_abs(k) + beta*AOD_MP_sca(k) &
                   + gam*Phi_IN_MP(k)
      PLF_total(k) = clamp(PLF_total(k), -0.8, 1.5)
    END DO
  END SUBROUTINE compute_PLF_profiles

  !> Adds the additional shortwave heating tendency.
  SUBROUTINE add_shortwave_heating_tendency_v12(Iuv_peak,  &
      kappa, eta_eff, f_metal, QEF, SWF, FAF, rho, cp, z,  &
      AOD_MP_abs, AOD_MP_sca, theta_tend)
    REAL, INTENT(IN)  :: Iuv_peak, kappa, eta_eff, QEF, SWF, FAF
    REAL, INTENT(IN)  :: rho(:), cp, z(:)
    REAL, INTENT(IN)  :: f_metal(:), AOD_MP_abs(:), AOD_MP_sca(:)
    REAL, INTENT(INOUT) :: theta_tend(:)
    REAL :: I_uv_avg, Qdot_PV, Qdot_PV_MP, S_cluster, adjust
    INTEGER :: k, nz

    nz = SIZE(z)
    I_uv_avg = 0.08 * Iuv_peak * kappa

    DO k=1,nz
      S_cluster = weight_layer_scalar(z(k), 950.0, 800.0)
      Qdot_PV   = I_uv_avg * eta_eff * f_metal(k) * QEF * SWF &
                 * FAF * S_cluster
      adjust    = MAX(0.0, 1.0 + 1.0*AOD_MP_abs(k) - 0.4*AOD_MP_sca(k))
      Qdot_PV_MP= Qdot_PV * adjust
```

```
      theta_tend(k) = theta_tend(k) + Qdot_PV_MP / (rho(k) * cp)
    END DO
  END SUBROUTINE add_shortwave_heating_tendency_v12

  !> Modifies the autoconversion threshold based on PCI_star.
  SUBROUTINE microphysics_autoconversion_v12(qc, qc_crit, PCI, &
      PLF_total_avg, lambda, autoconvert_flag)
    REAL, INTENT(IN) :: qc, qc_crit, PCI, PLF_total_avg, lambda
    LOGICAL, INTENT(OUT) :: autoconvert_flag
    REAL :: PCI_star, qc_crit_prime
    PCI_star      = PCI * (1.0 + PLF_total_avg)
    qc_crit_prime = qc_crit * (1.0 + lambda * PCI_star)
    autoconvert_flag = (qc > qc_crit_prime)
  END SUBROUTINE microphysics_autoconversion_v12

  !> Helper function for a triangular weighting profile.
  PURE FUNCTION weight_layer_scalar(z_hPa, z_bot, z_top) RESULT(w)
    REAL, INTENT(IN) :: z_hPa, z_bot, z_top
    REAL :: mid, half, w
    mid  = 0.5*(z_bot + z_top)
    half = 0.5*ABS(z_bot - z_top)
    IF (z_hPa >= z_top .AND. z_hPa <= z_bot) THEN
      w = 1.0 - ABS(z_hPa - mid)/half
    ELSE
      w = 0.0
    END IF
  END FUNCTION weight_layer_scalar

END MODULE micro_pv_resonance_v12
```

Listing 1: WRF/ICON Patch Stubs v1.2 — Microplastics (PLF) integrated

Appendix S3: Preregistered tests (subset)

Table 3: Subset of preregistered tests for ARF-Core validation.

Test ID	Hypothesis	Pass/Fail criterion
T1 (Skill)	ARF-augmented > Baseline	ΔAUC $\geq$ 0.05 oos (95% CI excludes 0)
T2 (IRB)	IRB peak precedes RI	Peak in [6,18] h lead; phase-lock vs. OLR min
T3 (Inter.)	Super-additivity	$\beta_{4:6} > 0$ with bootstrap CI
T4 (ERC HR)	Persistent AOD_{IR}raises hazard	Cox HR > 1 (95% CI) in 50–150 km ring
T5 (NegCtrl)	SAL ordering	BC/VOC > clean > SAL in ΔAUC

Appendix S4: Response to external critiques (summary)

- **Resonance metaphor** → formalized via gated interactions (Eq. 1), testable coefficients.
- **Synthetic figures** → all labeled *illustrative, synthetic*; preregistered real-data tests in S3.
- **Scope breadth** → this paper limits to RI; AMOC/trades deferred.

References

[1] Yin Li, Brian J. Soden, G. Saffi, and Y. Li. Anthropogenic forcing dominates the recent increase in rapid intensification of tropical cyclones. *Nature Communications*, 2023. doi:10.1038/s41467-023-40605-2.

[2] K. Bhatia, B. Bhatia, G. A. Vecchi, and T. R. Knutson. Recent increases in tropical cyclone intensification rates. *Nature Communications*, 2019. doi:10.1038/s41467-019-08471-z.

[3] C. Zhao, K. Zhang, and Y. Yang. Aerosol-induced radiative heating in the middle troposphere accelerates tropical cyclone intensification. *PNAS*, 2021. doi:10.1073/pnas.2013584117.

[4] B. H. Samset and G. Myhre. Vertical dependence of black carbon, sulphate and biomass burning aerosol radiative forcing. *Atmospheric Chemistry and Physics*, 2011. doi:10.5194/acp-11-11539-2011.

[5] A. Khain, M. Pinsky, and N. Benmoshe. Aerosol effects on the microphysics and dynamics of cloud and precipitation formation. *Surveys in Geophysics*, 2018. doi:10.1007/s10712-018-9477-7.

[6] D. Rosenfeld, Y. Zhu, M. Wang, Y. Zheng, T. Goren, and S. Yu. Aerosol-driven droplet concentrations dominate coverage and water of oceanic low-level clouds. *Science*, 363(6427), 2019. doi:10.1126/science.aav0566.

[7] Z. Meng et al. Spontaneous formation of reactive oxygen species and organic molecules in pristine water microdroplets. *Science Advances*, 2025. preprint; accessed 2025-09-30.

[8] X. Wen, G. Catalan, et al. Flexoelectricity in ice. *Nature Physics*, 2025. preprint; accessed 2025-09-30.

[9] AP News. Stronger, bigger hurricane erin forecast to create dangerous surf along us coast. press coverage, August 2025.

[10] ZDFheute. Super-taifun "ragasa" erreicht philippinen. press coverage, September 2025.

[11] The Weather Channel. Tropical storm gabrielle forecast to become a hurricane. press coverage, September 2025.

[12] David Zauner. Studie: Die atlantikströmung wankt, kippt und kollabiert. press coverage, August 2025.

[13] Helmholtz Centre for Environmental Research - UFZ. Press release: Underrated marine polluters - more nanoplastics in the ocean than expected. press coverage, July 2025.

[14] D. Ciutara, F. Ma, and H. Liu. Nanoplastic-induced changes in sea surface microlayer rheology and their impact on gas exchange. *Physical Chemistry Chemical Physics*, 2025.

[15] Nadja Podbregar. Pazifik: Wichtige meeresströmung ist ausgefallen, September 2025. Press coverage based on PNAS (2025).

[16] V. Dakos, E. H. van Nes, and M. Scheffer. Critical slowing down as a resilience metric for earth system tipping elements. *PNAS*, 2012.

[17] T. Woollings, B. Hoskins, and L. Shaffrey. The effect of the north atlantic oscillation on european blocking. *Geophysical Research Letters*, 2008. doi:10.1029/2008GL035088.

[18] C. W. J. Granger. Investigating causal relations by econometric models and cross-spectral methods. *Econometrica*, 1969. doi:10.2307/1912791.